Retrieval of stratospheric temperatures from Atmospheric Infrared Sounder radiance measurements for gravity wave studies

L. Hoffmann[1] and M. J. Alexander[2]

Received 3 October 2008; revised 19 December 2008; accepted 29 January 2009; published 4 April 2009.

[1] The Atmospheric Infrared Sounder (AIRS) on board the National Aeronautics and Space Administration's (NASA's) Aqua satellite has been continuously measuring mid-infrared nadir and sub-limb radiance spectra since summer of 2002. These measurements are utilized to retrieve three-dimensional stratospheric temperature distributions by applying a new fast forward model for AIRS and an accompanying optimal estimation retrieval processor. The retrieval scheme presented in this article does not require simultaneous observations of microwave instruments like the AIRS operational analyses. Instead, independent retrievals are carried out at the full horizontal sampling capacity of the instrument. Horizontal resolution is enhanced by a factor 3 in along- and across-track directions compared with the AIRS operational data. The total retrieval error of the individual temperature measurements is 1.6 to 3.0 K in the altitude range from 20 to 60 km. Retrieval noise is 1.4 to 2.1 K in the same vertical range. Contribution of a priori information to the retrieval results is less than 1% to 2% and the vertical resolution of the observations is about 7 to 15 km. The temperature measurements are successfully compared with ECMWF operational analyses and AIRS operational Level 2 data. The new temperature data set is well suited for studies of stratospheric gravity waves. We present AIRS observations of small-scale gravity waves induced by deep convection near Darwin, Australia, in January 2003. A strong mountain wave event over the Andes in June 2005 is analyzed in detail. Temperature perturbations derived from the new data set are compared with results from the AIRS operational Level 2 data and coincident measurements of the High Resolution Dynamics Limb Sounder (HIRDLS). The new retrieval does not show response to wave perturbations if the vertical wavelength is below 10 km. For 15 km vertical wavelength, the amplitudes are damped by a factor of two. For vertical wavelengths of greater than 20 km, AIRS shows very similar wave structure to HIRDLS and also has the advantage of providing horizontal phase front information. Data from the new full-resolution retrieval are far more suitable for gravity wave studies than results from the AIRS operational analysis.

Citation: Hoffmann, L., and M. J. Alexander (2009), Retrieval of stratospheric temperatures from Atmospheric Infrared Sounder radiance measurements for gravity wave studies, *J. Geophys. Res.*, *114*, D07105, doi:10.1029/2008JD011241.

1. Introduction

[2] Atmospheric waves transport momentum from lower to higher altitudes and have important effects on the general circulation. Small-scale waves called gravity waves (or buoyancy waves) are generally unresolved or poorly resolved in most global models, yet they are known to have profound effects on the circulation, temperature structure, and chemistry of the middle atmosphere [*Lindzen*, 1973; *Fritts and Alexander*, 2003; *Eyring et al.*, 2007]. Despite their small-scale and tendency to occur in localized wave packets, their collective effects are global in scale. With the advent of high-resolution temperature measurements from space researchers began to characterize the properties of gravity waves globally [e.g., *Fetzer and Gille*, 1994; *Wu and Waters*, 1996; *Eckermann and Preusse*, 1999; *Tsuda et al.*, 2000; *Preusse et al.*, 2000; *Wu*, 2004; *Wu et al.*, 2006; *Preusse et al.*, 2008].

[3] Satellite observations determine the temperature amplitudes or temperature variance associated with atmospheric gravity waves. The properties needed to characterize the gravity wave effects on the circulation are the wave pseudomomentum flux and the propagation properties of the waves. If these can be determined in the lower stratosphere, then the eventual effects of the waves on the circulation of the middle atmosphere can be estimated. The satellite observations of wave temperature amplitude do not generally include sufficient information about the waves to determine their propagation and pseudomomen-

[1]Institut für Chemie und Dynamik der Geosphäre, Forschungszentrum Jülich GmbH, Juelich, Germany.
[2]Colorado Research Associates Division, NorthWest Research Associates, Inc., Boulder, Colorado, USA.

0148-0227/09/2008JD011241

tum flux, because in addition to temperature amplitude, the wave horizontal and vertical wavelengths must be locally determined along with the wave propagation directions. All of the needed wave properties have been determined in some case studies of mountain waves observed from space [*Eckermann and Preusse*, 1999; *Preusse et al.*, 2002; *Alexander and Teitelbaum*, 2007; *Eckermann et al.*, 2007]. Global estimates of wave pseudomomentum flux have been made using satellite observations [*Ern et al.*, 2004, 2006; *Alexander et al.*, 2008], however these had large uncertainties because the propagation directions of the waves could not be determined.

[4] Measurements from the Atmospheric Infrared Sounder (AIRS) [*Aumann et al.*, 2003] on the Aqua satellite [*Parkinson*, 2003] provide high-resolution swaths that allow imaging of horizontal wavelengths and propagation directions for gravity wave packets in the stratosphere from radiance measurements in CO_2 emission channels [*Alexander and Barnet*, 2007]. Wave vertical wavelengths and temperature amplitudes of the waves can be determined from the AIRS retrieved temperatures, however the AIRS operational retrievals (Level 2 data) degrade the native resolution of the radiance measurements by factors of 3×3 (along-track $\times$ cross-track) in order to perform cloud clearing and extend the retrievals into the troposphere [*Barnet et al.*, 2003; *Susskind et al.*, 2003; *Cho and Staelin*, 2006]. This resolution degradation eliminates many of the features of gravity waves observed in the stratospheric radiances.

[5] In the present article, we describe a stratosphere-only retrieval of atmospheric temperature at the full native resolution of the AIRS radiance measurements and examine some case studies of stratospheric gravity wave events. The retrieval uses information measured by the AIRS instrument only, unlike the operational Level 2 retrieval which also requires AMSU (Advanced Microwave Sounding Unit) measurements. We compare the full-resolution retrievals to the Level 2 temperature data, and we validate the wave structures via comparison to measurements from the High Resolution Dynamics Limb Sounder (HIRDLS) [*Gille et al.*, 2003; *Gille et al.*, 2008] instrument on the Aura satellite. Both HIRDLS-Aura and AIRS-Aqua fly in the A-Train satellite constellation [*Schoeberl et al.*, 2004], so HIRDLS and AIRS observe the same wave events with less than 100 minute time difference. To ensure minimum changes in the wavefield in this time, we examine stationary mountain wave events for the validation.

2. AIRS Operational Data Products

[6] The AIRS instrument has provided nearly continuous measurement coverage since May 2002. In this article we restrict ourselves to measurements where consolidated Level 1B and Level 2 data products are available from NASA (processing software version 5.x). The aim of the NASA operational Level 1B data processing is to convert instrument raw data to calibrated radiance spectra and corresponding geolocation data [*Aumann et al.*, 2000]. The Level 2 processing aims on retrieval of atmospheric parameters from the AIRS radiance measurements. Details are described by *Goldberg et al.* [2003], *Rosenkranz* [2003], *Susskind et al.* [2003, 2006], and *Strow et al.* [2003, 2006]. Comprehensive pre-flight and permanent in-flight calibrations were carried out to guarantee a high quality AIRS Level 1B data product [*Pagano et al.*, 2003; *Aumann et al.*, 2006; *Nalli et al.*, 2006; *Tobin et al.*, 2006a; *Walden et al.*, 2006]. The AIRS atmospheric data products have been validated by comparison with independent measurements obtained by other remote-sensing and in situ experiments [e.g., *Fetzer et al.*, 2003; *Divakarla et al.*, 2006; *Tobin et al.*, 2006b]. For an overview of validation activities see the study by *Fetzer* [2006], and references therein. Our analysis uses both Level 1B and Level 2 data as input.

3. Forward Modeling for the AIRS Instrument

3.1. Fast Forward Model for AIRS

[7] Because of the large amount of data, a fast forward model is essential to comprehensively analyze AIRS radiance measurements. The forward model combines a radiative transfer code, which requires most of the computational time, with a specific instrument model. Within the retrieval process the forward model is iteratively called to simulate the measurements AIRS would make for a given atmospheric state. The retrieved atmospheric state is determined when simulated observations and real measurements are in agreement. For the temperature retrievals presented here we adapted the Juelich Rapid Spectral Simulation Code (JURASSIC) [*Hoffmann*, 2006] for forward modeling.

[8] In this study the radiative transfer model does not have to simulate scattering of solar or atmospheric radiance at the ground or at the top of clouds because we only include AIRS channels for which the radiance entirely originates in the stratosphere. For raypaths in clear air, scattering can be neglected because of the small infrared scattering cross-sections. JURASSIC computations are based on the assumption of local thermodynamic equilibrium (LTE). This limits the analysis of daytime measurements to the AIRS 15 μm temperature channels since non-LTE effects caused by solar excitation of CO_2 molecules are present in the 4 μm temperature channels [*de Souza-Machado et al.*, 2006; *Strow et al.*, 2006]. For nighttime measurements non-LTE effects have not been observed in AIRS data and all stratospheric channels can be utilized for the retrievals.

[9] The JURASSIC forward model provides a flexible handling of different types of observation geometries (e.g., nadir, sub-limb, limb, or zenith) and different types of atmospheric input data (e.g., single vertical profiles, set of profiles along a satellite track, and regular or irregular 3D model data). This is achieved by providing several interpolation functions for atmospheric data as well as a flexible ray-tracing routine [*Hase and Höpfner*, 1999] which determines the atmospheric raypaths iteratively, based on a given observer position and an initial tangent vector. Ray-tracing takes into account refraction, i.e., the bending of raypaths toward the Earth due to increasing atmospheric density and refractivity at lower altitudes. The refractive index of air is obtained from a formula adopted by the International Association of Geodesy in 1999, based on the study by *Ciddor* [1996]. JURASSIC was previously used to model limb-observation geometries [e.g., *Hoffmann*, 2006; *Hoffmann et al.*, 2008], but is now also adapted to the specific requirements of the AIRS measurement geometry.

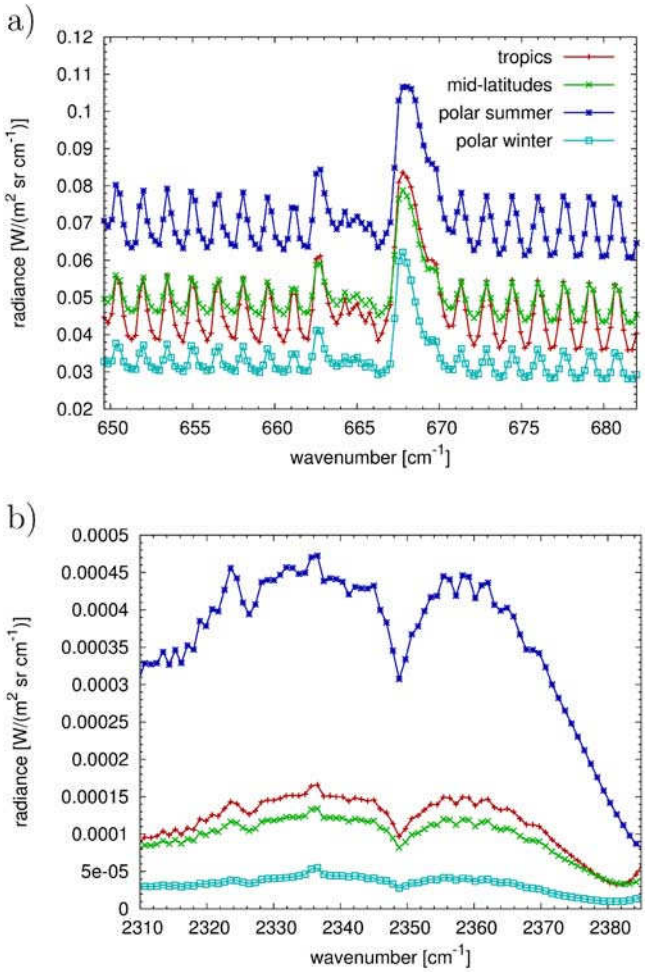

Figure 1. JURASSIC forward model simulations for (a) the 15 μm and (b) the 4 μm temperature channels of AIRS. Curves are for different atmospheric conditions [*Remedios et al.*, 2007], see legend in Figure 1a.

[10] JURASSIC computes the radiative transfer based on the emissivity growth approximation (EGA) [*Weinreb and Neuendorffer*, 1973; *Gordley and Russel*, 1981; *Marshall et al.*, 1994; *Francis et al.*, 2006]. A large reduction of CPU time is achieved, since the radiative transfer is not computed based on the conventional line-by-line approach, but by operating on spectral mean values of emissivity, Planck function, and radiance. Spectral mean emissivities are obtained by fast interpolation from pre-computed look-up-tables. The emissivity look-up-tables are derived from exact line-by-line calculations, utilizing the Reference Forward Model (RFM) [*Dudhia*, 2004]. To further improve model accuracy a linear regression scheme is applied which uses the EGA radiances as well as channel-dependent radiometric offsets as error predictors. The regression coefficients are obtained by least squares fitting a linear model to the radiance residuals between uncorrected JURASSIC calculations and line-by-line reference model output.

[11] As an example, Figure 1 shows the results of JURASSIC forward model simulations for the 4 μm and 15 μm temperature channels of AIRS. The simulations include only AIRS channels where radiance emissions of carbon dioxide dominate, and contributions of interfering species or aerosols can be neglected in comparison with noise. Computations are carried out for pressure and temperature data for four different atmospheric conditions [*Remedios et al.*, 2007]. The CO_2 volume mixing ratio is set to 370 ppm. The upper boundary of the atmosphere is set to 90 km. The forward model simulations show highest radiances in the polar summer atmosphere, followed by mid latitudes and tropics, and lowest radiances in the polar winter atmosphere. Because of increased sensitivity of the Planck function to temperature changes at decreasing wavelength [e.g., *Dudhia*, 2003], the radiance varies with the atmospheric conditions by a factor 1.7 to 2.3 in the 15 μm channels and by a factor 6 to 15 in the 4 μm channels. Temperature may be more accurately retrieved at shorter wavelengths in general.

3.2. Reference Model Comparison

[12] The most important parameter for the accuracy and performance of JURASSIC is the ray-tracing step size. The larger the step size the faster the computations are carried out. Over a wide range of step sizes Δs the CPU time t follows $t \sim 1/\Delta s$, that is, doubling the step size leads to half the CPU time etc. However, the maximum step size is limited because the atmospheric inhomogeneity along the raypaths needs to be sampled sufficiently. We find that for most atmospheric conditions the forward model errors remain below 0.2% for 0.5 km step size and are then negligible compared with AIRS noise. The CPU time for the AIRS forward calculations is about a factor 1000 faster than line-by-line computations with the reference model in this case.

[13] The approximations used to accelerate the radiative transfer calculations deteriorate the model accuracy. These errors remain small if the spectral variations of the derivative of transmittance along the path are uncorrelated with that of the Planck function [*Rodgers*, 2000]. The actual forward model errors need to be quantified by comparison with line-by-line reference calculations. For pure EGA calculations the model errors are on the order of the AIRS noise (Figures 2a and 2b). Larger EGA errors are observed in some 4 μm channels in the polar summer atmosphere where radiance intensities are highest. The mean relative errors are -0.3 to 1.4% in the 15 μm channels and -2.0 to 1.8% in the 4 μm channels. These values correspond with results of *Gordley and Russel* [1981] and *Marshall et al.* [1994] who studied the accuracy of the EGA for a wide set of applications.

[14] A common approach to improve the accuracy of radiative transfer models based on the EGA is to average radiances or transmittances derived by the EGA with results obtained by the Curtis-Godson approximation (CGA) [e.g., *Marshall et al.*, 1994; *Francis et al.*, 2006]. The errors of the two methods are often in the same order, but of opposite sign, that is, an average EGA/CGA solution provides better accuracy. However, for the AIRS application only minor improvements were found with this approach. A disadvantage of the combined EGA/CGA solution is the enhanced computational overhead (about 50% increase in CPU time). Another approach to improve model accuracy are regression schemes [e.g., *Francis et al.*, 2006]. Figures 1, 2a, and 2b indicate that the EGA errors are clearly correlated with radiance intensity. Hence we implemented a simple linear

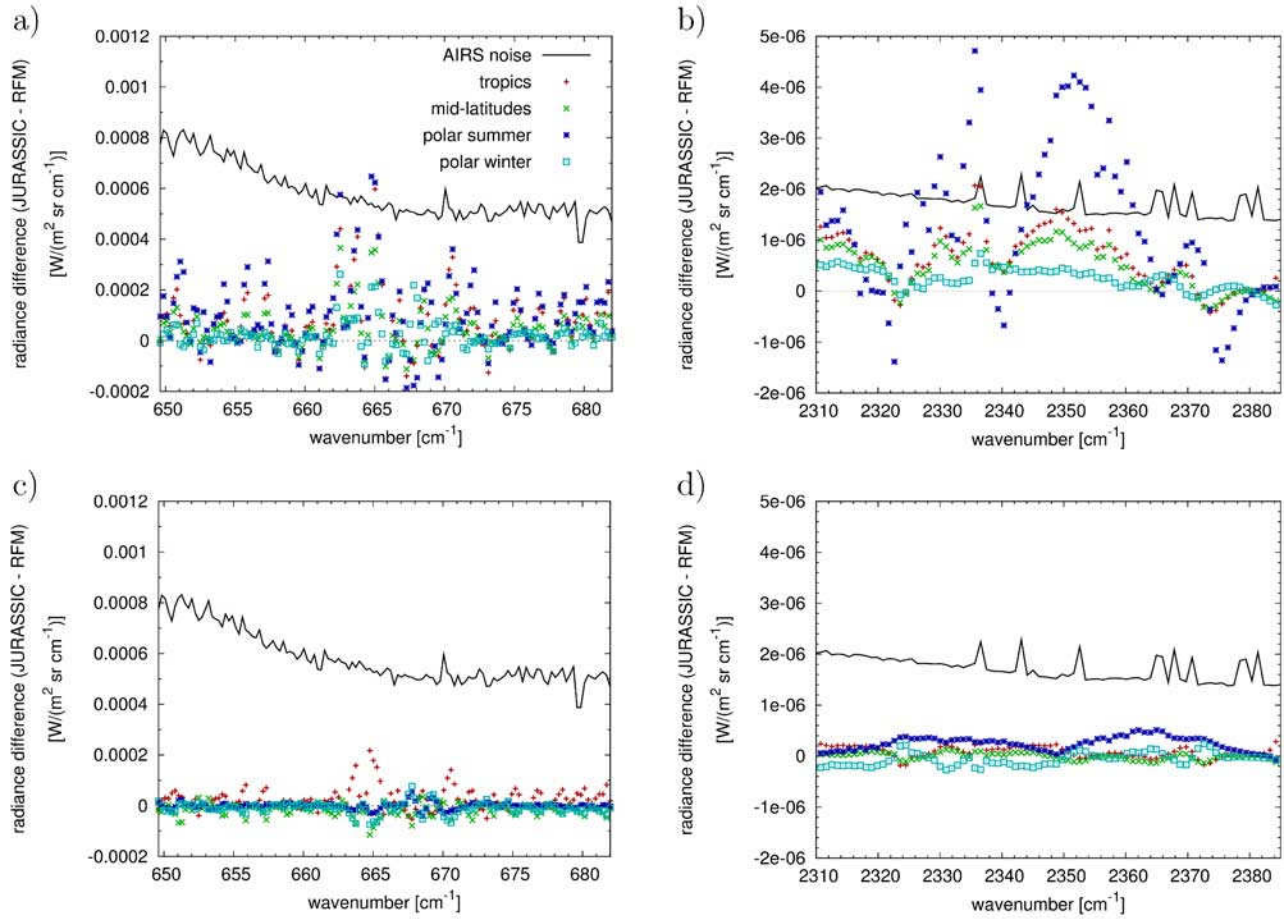

Figure 2. Comparison of JURASSIC and RFM simulations for (a, c) the 15 μm and (b, d) the 4 μm temperature channels of AIRS. Symbols are for different atmospheric conditions [*Remedios et al.*, 2007], see legend in Figure 2a. The black curves indicate the AIRS noise. Plots in Figures 2a and 2b show the EGA errors. Plots in Figures 2c and 2d show the residuals after model errors have been corrected by linear regression.

regression scheme and parameterized the radiance errors as functions of the EGA radiance intensities and constant radiometric offsets for each AIRS channel. This effectively removes the model bias and further corrects by means of optimized linear scaling factors. The relative errors are reduced to -0.2 to 0.4% in the 15 μm channels and -0.7 to 1.3% in the 4 μm channels (Figures 2c and 2d). The remaining model errors are well below the AIRS noise. The computational overhead due to the regression is insignificant.

3.3. Temperature Kernel Functions

[15] The temperature kernel functions indicate how the individual channels of the AIRS instrument respond to gravity waves or any other perturbation of the temperature profile. Temperature kernel functions are computed here by means of numerical perturbation, i.e., by determining the radiance difference between two forward calculations, where one temperature profile is perturbed by a triangular shape with 2 km baseline and 1 K maximum centered on a given altitude. The results for midlatitude atmospheric conditions and the nadir viewing direction are shown in Figures 3a and 3b. There is only a weak dependence of the temperature kernel functions on the AIRS scan angle. However, the results depend on the atmospheric state due to the non-linearity of the forward model.

[16] Except for the strong CO_2 Q branch at 667 to 670 cm^{-1} the 15 μm temperature kernel functions peak at 17 to 27 km and have a full width at half maximum (FWHM) of 9 to 15 km. The 4 μm channels typically peak at 25 to 40 km and have a FWHM of 19 to 28 km. The temperature kernel functions of the 15 μm channels depend on individual strong CO_2 spectral lines. If a strong line is present in the channel it gets optically thick in the mid stratosphere. Otherwise, the temperature kernel functions peak lower down. In contrast, the AIRS spectral response functions for the 4 μm channels are broader and cover rather different monochromatic optical depths. This causes a vertical broadening of the kernel functions. The 4 μm channels provide less information about the vertical structure of the temperature profile, but are included in the retrieval since they help to reduce noise.

3.4. Response to Wave Perturbations

[17] A study about the response of AIRS forward model simulations to various wave perturbations of the temperature profile helps to identify the AIRS channels which are most suited to analyze stratospheric gravity waves. To

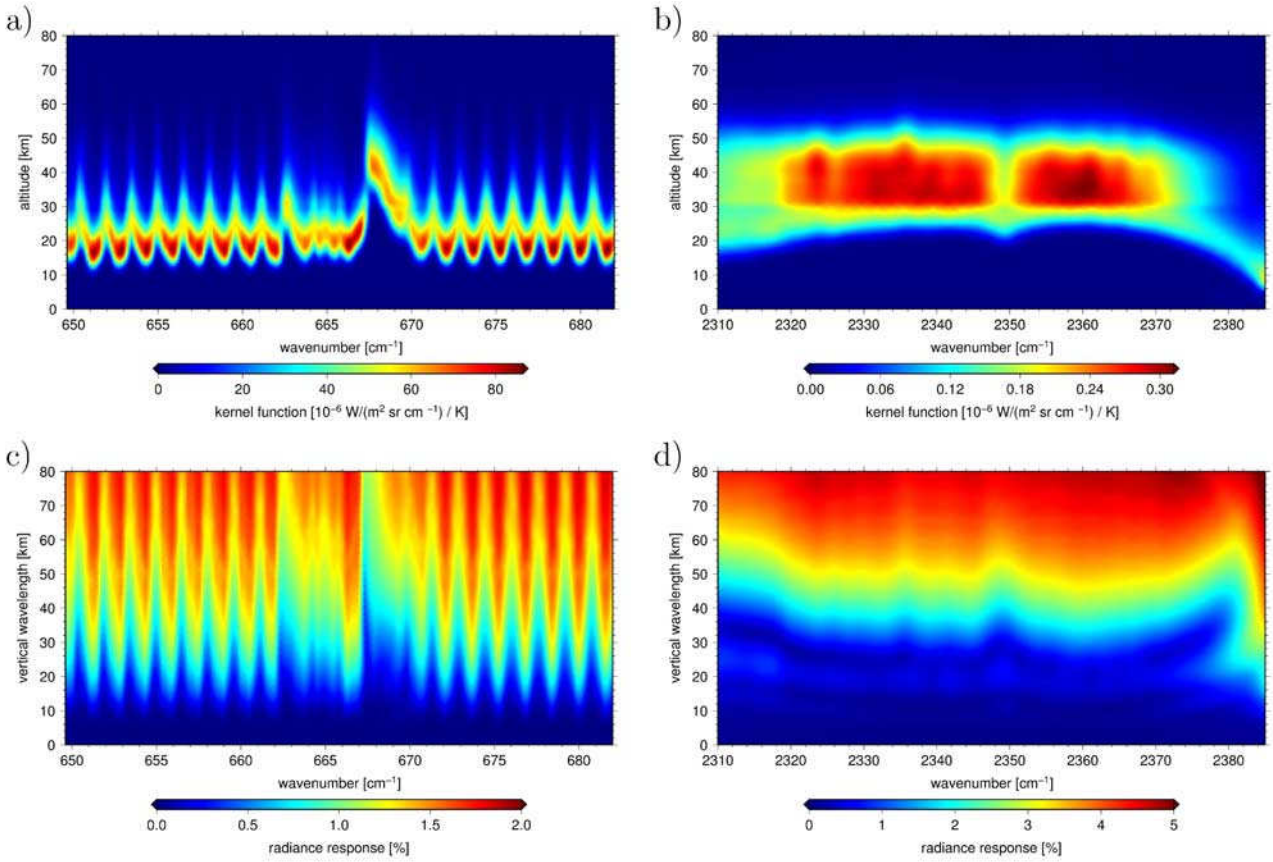

Figure 3. Upper row shows temperature kernel functions for (a) the 15 μm and (b) the 4 μm stratospheric temperature channels of AIRS. Lower row shows the maximum response to 1 K wave perturbations of the temperature profile in forward model calculations for (c) the 15 μm and (d) the 4 μm channels. All computations are based on midlatitude atmospheric conditions and the nadir viewing direction.

derive the response of an individual AIRS channel to a wave perturbation of the background temperature profile the perturbation profile needs to be convolved with the temperature kernel function. Alternatively, the response can be calculated directly by differencing the simulated radiances for the perturbed and unperturbed temperature profile. The direct approach is more accurate in case of large perturbations (10 K or more) because it does not rely on the linearity of the forward model and is used here. A comparison of both methods allows to infer the degree of non-linearity of the retrieval problem.

[18] Figures 3c and 3d show the maximum response of the AIRS stratospheric channels to temperature wave perturbations with 1 K amplitude for various vertical wavelengths. The maximum response was determined by varying the wave phase. The plots show relative response, i.e., radiance difference divided by intensity. Comparing the observed response to the AIRS noise (i.e., about 1% for the 15 μm channels and 1.5% for the 4 μm channels) shows that a 1 K wave amplitude is close to the detection limit of most channels. The relative response is generally higher in the 4 μm channels and weaker in the 15 μm channels due to the varying sensitivity of the Planck function to temperature changes in these spectral regions (see section 3.1).

[19] The response is practically zero below 10 km vertical wavelength, but increases rapidly for larger values. Vertical wavelengths below 10 km are smaller than the FWHM of all stratospheric temperature kernel functions. In this case the positive and negative perturbations of the temperature profile and the corresponding radiance contributions cancel out. For intermediate wavelengths the contributions do not cancel out completely and some response will be observed. In general, the response increases more rapidly if the FWHM of the temperature kernel functions are small. The maximum response occurs when the vertical window defined by the temperature kernel function is entirely filled by one positive amplitude of the wave with a wavelength much longer than the FWHM.

[20] The interpretation of AIRS radiance perturbations in individual terms of temperature requires foreknowledge of the wave vertical wavelength. A temperature retrieval that optimally combines information from multiple radiance channels will give the vertical temperature structure, allowing direct determination of the vertical wavelength, as well as quantifying vertical resolution and retrieval error.

4. Retrieval of Stratospheric Temperature Data

4.1. Channel Selection

[21] An optimized set of AIRS channels needs to be identified for the stratospheric temperature retrievals. Starting from a list containing all 4 and 15 μm temperature channels (649.62 to 681.993 cm^{-1} and 2299.8 to

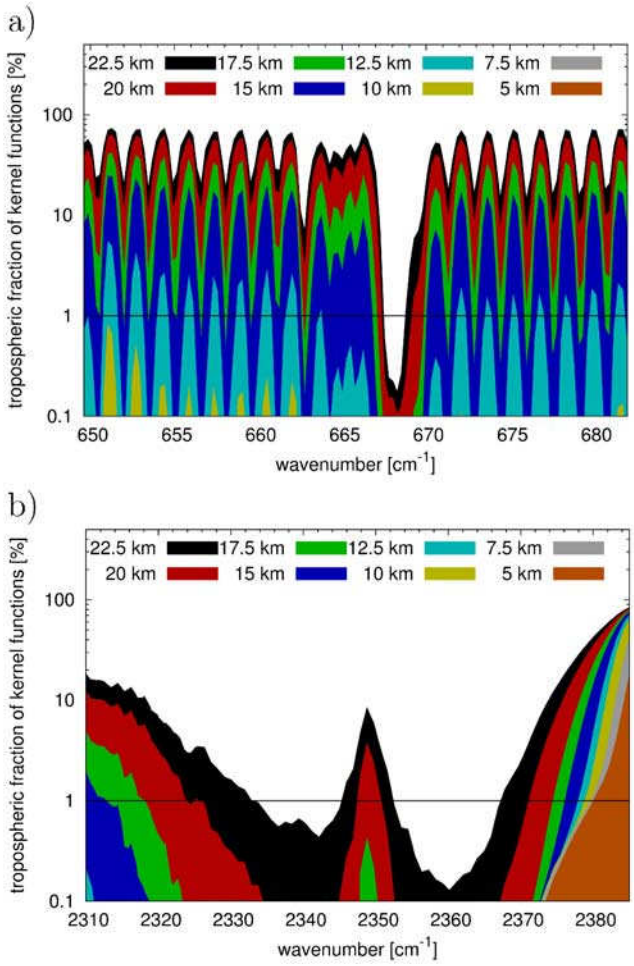

Figure 4. Tropospheric fraction of the area of (a) the 15 μm and (b) the 4 μm temperature kernel functions. Data are for midlatitude atmospheric conditions. Colored curves are for different tropopause altitudes (see legend). The black line indicates the 1% threshold used to determine the cloud-free channels.

2422.85 cm^{-1}) first the channels which cannot be used due to detector failures or other instrument problems are removed. Next we remove channels that show significant radiance emissions of tropospheric clouds. The remaining channels are sorted in order to maximize the Shannon information content.

[22] The temperature kernel functions discussed in section 3.4 can be used to identify channels which may be influenced by tropospheric clouds. Figure 4 shows the tropospheric fraction of the area of the temperature kernel functions for various tropopause heights. To identify cloudy channels a specific threshold for tropospheric fraction of the kernel functions and a maximum tropopause height need to be selected. The maximum tropopause height is set to 17.5 km, according to satellite observations [e.g., *Wang et al.*, 1996; *Spang et al.*, 2002]. The threshold for the maximum tropospheric fraction of the temperature kernel functions is set to a very low value of 1%, to ensure that radiance contributions of tropospheric clouds can be neglected compared with noise.

[23] After preselection, 78 AIRS channels remain suitable for the stratospheric temperature retrievals. These channels are sorted according to their contribution to Shannon information content. The Shannon information content measures the reduction of the entropy of the a posteriori probability density function compared with the a priori probability density function. It measures how uncertainty in knowledge about the state variables is reduced by the retrieval. This study closely follows the work of *Rodgers* [1998], *von Clarmann and Echle* [1998], and *Dudhia et al.* [2002]. We optimize only for midlatitude atmospheric conditions, however tests with other atmospheric conditions do not show significant changes in the list of channels. Since the 4 μm channels need to be excluded for daytime retrievals (non-LTE effects), the 4 and 15 μm channels are optimized separately.

[24] The optimized lists of AIRS stratospheric temperature channels are shown in Tables 1 and 2. The tables list the centroid wave number $\bar{\nu}$ of the channels and the ratio $H/H_{\max}$ of the accumulated Shannon information content versus total information content. The channels are sorted in order to maximize this quantity. The tables also indicate the growth in degrees of freedom for signal Δd_s which is obtained by adding each individual channel. The degrees of freedom for signal d_s represent the number of altitude levels with independent information. While optimizing the Shannon information content means to minimize the retrieval errors, optimizing the degrees of freedom for signal means to optimize the resolution of the retrievals. However, we can confirm the result of *Rodgers* [1998], that both approaches lead to nearly identical results. For reference, the tables also show the noise of the individual channels. In addition, the tables list the altitude $z_{\max}$ where the temperature kernel functions peak and their FWHM (see section 3.3).

[25] Since noise scales with $1/\sqrt{n}$ the growth of Shannon information content rapidly slows down with an increasing number n of radiance channels. Selecting only the first two channels from each list already provides more than 50% of the total Shannon information content. Selecting the top 7 out of 12 channels (15 μm) or top 23 out of 66 channels (4 μm) will provide more than 90% of the total information content. For the retrieval we select all 15 μm channels to obtain the best result for daytime conditions, but add only the first 23 of the 4 μm channels for nighttime retrievals in order to reduce the computational effort. On a 1.8 GHz AMD Opteron(tm) core the retrieval of a granule based on

Table 1. Optimized List of 15 μm Stratospheric Temperature Channels

	$\bar{\nu}$ (cm^{-1})	$H/H_{\max}$ (%)	Δd_s	Noise (nW/[cm^2 sr cm^{-1}])	$z_{\max}$ (km)	FWHM (km)
1	668.53	36.7	1.00	50	35	18
2	669.55	59.0	0.98	48	28	16
3	667.77	75.9	0.87	51	41	13
4	667.52	80.4	0.33	51	43	15
5	669.80	85.0	0.19	49	28	18
6	668.03	88.1	0.16	50	41	14
7	668.79	90.8	0.11	52	31	20
8	667.27	93.3	0.07	52	27	12
9	662.76	95.3	0.21	56	28	14
10	668.28	97.2	0.05	50	39	17
11	669.04	98.8	0.09	51	28	16
12	669.29	100.0	0.03	50	27	14

Table 2. Optimized List of 4 μm Stratospheric Temperature Channels

	$\bar{\nu}$ (cm^{-1})	H/H_{max} (%)	Δd_s	Noise (nW/[cm^2 sr cm^{-1}])	z_{max} (km)	FWHM (km)
1	2356.35	35.6	1.00	0.15	41	22
2	2373.59	52.7	0.98	0.14	25	27
3	2335.63	61.6	0.78	0.18	41	25
4	2360.16	66.0	0.22	0.15	34	21
5	2348.77	69.2	0.09	0.15	26	29
6	2371.66	71.5	0.17	0.14	33	26
7	2359.21	73.6	0.10	0.15	38	21
8	2318.95	75.3	0.14	0.19	41	29
9	2336.56	77.0	0.04	0.22	41	25
10	2366.86	78.6	0.11	0.14	34	23
11	2323.56	80.1	0.17	0.19	41	25
12	2358.26	81.2	0.03	0.15	38	21
13	2369.74	82.3	0.09	0.15	41	26
14	2337.50	83.3	0.07	0.17	41	24
15	2372.63	84.3	0.01	0.14	27	27
16	2324.48	85.1	0.08	0.19	41	25
17	2357.30	86.0	0.04	0.15	34	22
18	2361.12	86.8	0.02	0.15	38	22
19	2334.70	87.5	0.02	0.18	41	25
20	2368.78	88.2	0.04	0.15	34	25
21	2319.87	88.8	0.02	0.19	41	28
22	2362.07	89.5	0.02	0.15	38	22
23	2363.03	90.1	0.02	0.15	34	22
⋮	⋮	⋮	⋮	⋮	⋮	⋮
65	2325.06	100.0	0.00	0.99	41	25
66	2321.99	100.0	0.00	0.99	41	26

35 channels requires about 8 h wall time while a setup including all 78 channels would require about 18 h.

4.2. Retrieval Scheme

[26] The retrieval of stratospheric temperature data from the AIRS radiance measurements presented in this article is based on the optimal estimation approach [*Rodgers*, 1976, 1990, 2000]. The maximum a posteriori solution of the inverse problem, that is, an estimate of the stratospheric temperature profile is found by minimizing the deviations between forward model simulations based on the current estimate of the state and actual radiance measurements, as well as minimizing the deviations between the estimate and an a priori state. Deviations are normalized by the measurement error covariance and the a priori covariance, respectively. Since our a priori covariance is tuned and does not exactly represent a real atmospheric ensemble, the obtained solution may not strictly be referred to as "optimal estimate" but as "obtained by Bayesian regularization". The retrieval problem is moderately non-linear (on scales above 10 K). A Levenberg-Marquardt approach neglecting the Hessian is applied to iteratively find the minimum of the cost function [*Rodgers*, 2000].

[27] For the temperature retrievals presented in this work we use a 1D scheme, assuming a homogeneously stratified atmosphere for each footprint. The individual retrievals are not influenced by the assumption of a homogeneously stratified atmosphere because every atmospheric layer is crossed only once by the raypath analyzed. Retrievals cover the altitude range 10 to 70 km. The height grid provides a 3 km sampling below 60 km altitude and 5 km sampling up to 90 km altitude. The vertical sampling in the stratosphere is similar to the AIRS operational retrieval grid. While temperature will be retrieved, pressure is recomputed based on the assumption of hydrostatic equilibrium. For the hydrostatic build-up we chose a reference altitude of 30 km, because this altitude is best covered by measurement information in our retrieval setup. The pressure at this altitude is obtained by using the geopotential heights reported in the AIRS operational Level 2 data. The AIRS geopotential heights depend on the operational temperature data and surface pressure data obtained from meteorological analyses (NCEP GFS forecasts).

[28] In the measurement error covariance, only noise is taken into account, it being the leading error term. All other error terms are ignored during the inversion process and estimated in an a posteriori manner [e.g., *Rodgers*, 1990; *von Clarmann et al.*, 2001]. Since noise is uncorrelated, the measurement error covariance matrix is diagonal. To initialize the full temperature a priori covariance matrix a first-order autoregressive model is applied [e.g., *Rodgers*, 2000]. The temperature standard deviation is set to 20 K, which exceeds the climatological variability by a factor 2 to 5 at 10 to 70 km altitude. We use high standard deviations to avoid over-constraining the retrievals. The first-order autoregressive model describes a Markov process or a variant of a random walk. Temperature departure from the mean at height level $i + 1$ is obtained from the departure at level i plus a random component. Because of this approach the correlations decay exponentially with the vertical distance of the atmospheric levels, see the study by *Rodgers* [2000] for details. The vertical correlation length is an important tuning parameter for the retrieval as it controls the trade-off between retrieval error and vertical resolution. This will be illustrated in the next section.

[29] Temperature data from the AIRS operational retrieval and from a measurement- and model-based climatology [*Remedios et al.*, 2007] are used to define the a priori state for the retrieval. We only consider AIRS operational data whose quality is rated "good" or "best". On each altitude level data gaps are filled by distance-weighted next-neighbor averaging. Above the top boundary of the operational retrieval (about 65 km) a smooth transition to

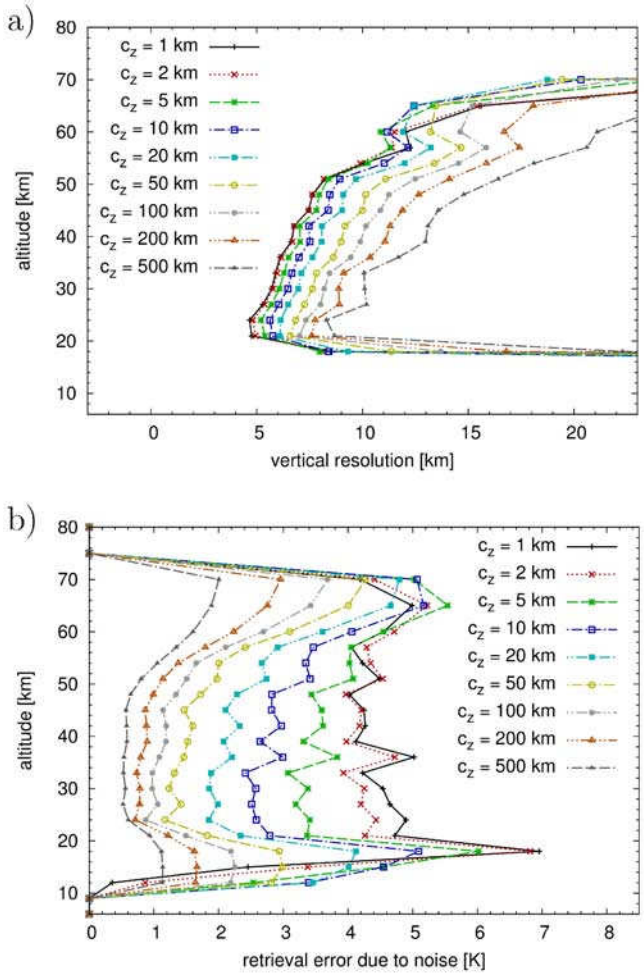

Figure 5. Dependence of (a) the vertical resolution of the temperature retrievals and (b) the retrieval errors due to noise on the vertical correlation length c_z of the a priori covariance. The correlation length c_z = 50 km has been selected for the retrievals. All calculations are based on midlatitude atmospheric conditions.

climatological data is achieved by linearly decreasing with altitude the temperature difference between the climatology and the operational data at the top boundary.

[30] One needs to be aware that correlated measurement data are used twice in the whole process. We use operational temperature data derived from cloud-cleared radiances as a priori information. The cloud-cleared radiances are derived from calibrated Level 1B radiance data. Thereby, cloud-clearing causes a degradation of horizontal resolution by a factor 3 × 3 in the derived data. On the other hand, the full-resolution Level 1B radiances are also used directly for our retrieval of stratospheric temperature. This is theoretically inappropriate in the context of optimal estimation [*Rodgers*, 2000]. However, we still do so for practical reasons. The first reason is, the operational data most likely will provide a better temperature estimate than any climatology for the altitudes not covered by our analysis. Hence the approach helps to reduce the retrieval errors due to uncertainties in top and bottom column data. The second reason is, since the a priori atmospheric state is used as the first guess for the iterative minimization, starting from a state close to the final solution helps to reduce the number of iterations required to find the solution and to reduce computational effort. We will show in the following section that our retrieval results are nearly free of a priori information in the stratosphere.

4.3. Influence of a Priori Information

[31] In order to determine the influence of a priori information on the retrieval results and to estimate the retrieval errors we study the diagnostics of idealized retrievals based on end-to-end tests. Using midlatitude climatological data [*Remedios et al.*, 2007], we first simulate AIRS measurements applying the forward model and then run retrievals on the simulated observations. Since we do not use actual measurements and do not simulate measurement or parameter errors, the diagnostics presented here will not be obscured by any individual retrieval error.

[32] The study shows that the vertical correlation length c_z used for the a priori covariance directly controls the trade-off between the vertical resolution of the observations (Figure 5a) and the retrieval error due to noise (Figure 5b). Noise can only be improved at the cost of reduced resolution and vice versa. We choose a vertical correlation length c_z of 50 km to obtain a data set which is best suited for gravity wave studies in terms of noise and resolution. For this value the resolution varies from 6.6 to 14.7 km while the noise is about 1.4 to 2.1 K at 20 to 60 km altitude. Reducing the vertical correlation length leads to noise levels to high for gravity wave analyses. The areas of the averaging kernels indicate that the amount of a priori information is below 1 to 2% in the same altitude range (not shown). The amount of a priori information exceeds 10% below 15 km and above 65 km.

[33] Since the response of the retrieval toward wave-like disturbances of the temperature profile is generally more complex than indicated by the simple resolution estimates presented in Figure 5a, the response itself is shown in Figure 6. There is no response to waves with vertical wavelengths below 9 km. For 15 km wavelength the disturbances are reproduced but the amplitude is damped by a factor 2. For 24 km vertical wavelength and larger values the wave-like disturbances are reproduced nearly exactly. At altitudes above 50 to 60 km the retrieved wave structures show an increase in vertical wavelength due to decreasing vertical resolution.

4.4. Error Analysis

[34] A retrieval error budget needs to be estimated for a complete characterization of the retrieval results. The error analysis presented here is based on the concept of linearization of the transfer function [*Rodgers*, 1990, 2000]. The transfer function describes the retrieval result as a function of the retrieval method, the forward model, the complete set of method and model parameters, and the true atmospheric state. The total retrieval error is composed of (1) the retrieval noise, (2) the forward model parameters errors, (3) the forward model errors, and (4) the smoothing error. By applying the transfer function concept, detailed error budgets for the AIRS temperature retrieval can be derived. The total retrieval error of the individual temperature data, including all statistical and systematic components, is estimated 1.6 to 3.0 K at 20 to 60 km altitude (Table 3). We will

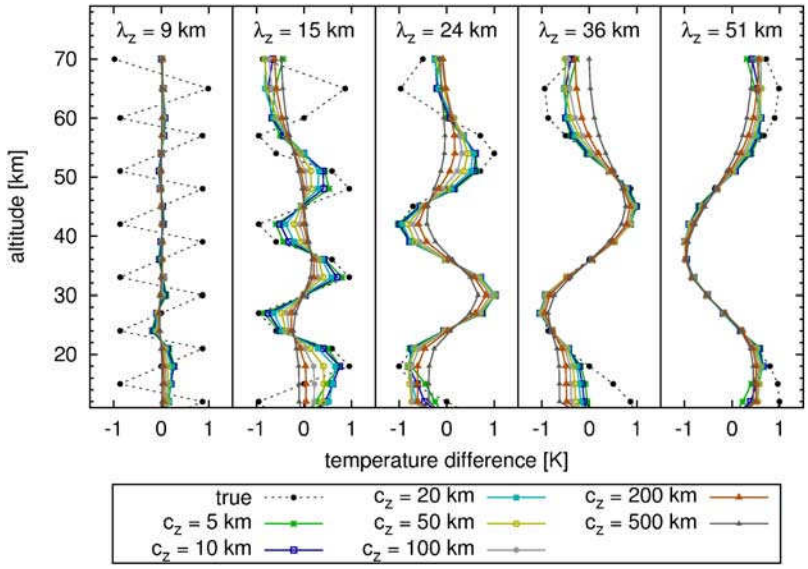

Figure 6. Response of the retrieval to wave-like disturbances of the temperature profile for various vertical wavelengths λ_z. The dashed curves show the true temperature perturbations. Solid colored curves are temperature perturbations obtained from retrieval results for different vertical correlation lengths c_z (see legend). The correlation length c_z = 50 km has been selected for the retrievals.

now discuss the individual components of the retrieval error budget in more detail.

[35] Noise is a main component of the total retrieval error. The retrieval noise is about 1.4 to 2.1 K within the altitude range where the retrieval provides reasonable results (20 to 60 km). This noise error is the most relevant error for gravity wave studies.

[36] The systematic errors increase from 0.6 K at 20 km altitude to 2.1 K at 60 km altitude. Compared to noise the systematic errors are less important for gravity wave studies, but need to be taken into account when comparing absolute values of temperature with other experiments. The dominating systematic error at upper altitudes is the top column error caused by uncertainty in temperature data above 60 to 70 km. The top column uncertainty is about 4 K at 65 km (AIRS operational data) and increases to the climatological uncertainty of about 25 K at 90 km. This uncertainty causes a temperature retrieval error of 1.6 K at 50 to 60 km altitude. Second, on the basis of an absolute radiometric accuracy of the AIRS measurements of about 12 mW/(m^2 sr cm^{-1}) for the 15 μm temperature channels and 0.06 mW/(m^2 sr cm^{-1}) for the 4 μm temperature channels [*Pagano et al.*, 2003], we estimate a retrieval error of 0.4 to 0.6 K. Third, a reference pressure uncertainty for the hydrostatic build-up of 5% (corresponding to 400 m uncertainty of the geopotential heights) will cause a retrieval error of 0.3 to 0.9 K. Fourth, a 5% uncertainty in the carbon dioxide spectroscopic data [*Rothman et al.*, 2003] causes retrieval errors of 0.1 to 0.4 K. Fifth, the carbon dioxide volume mixing ratio has an annual variability of about 3% and a growth rate of about 2 ppm/year [e.g., *Aumann et al.*, 2005] which are neglected in our setup. This leads to systematic retrieval errors of 0.1 to 0.2 K. Finally, the approximated computation of the radiative transfer in the fast forward model causes retrieval errors of 0.2 to 0.3 K (compare Figure 2 for the fast forward model errors).

5. Temperature Measurements and Validation

5.1. Consistency of the Retrieval With the Measurements

[37] The consistency of the retrieved measurements with the AIRS radiance observations is routinely tested to check that the non-linear retrievals do not converge against spurious minima. The retrieved measurements are calculated by applying the forward model on the retrieved temperature profiles. The radiance residuals are divided by the corresponding noise values of the AIRS channels.

[38] As an example, Figure 7 shows a histogram of normalized radiance residuals from an individual AIRS

Table 3. Temperature Retrieval Errors for Midlatitude Atmospheric Conditions

Height Range (km)	Total Error[a] (K)	Noise Error (K)	Systematic Errors[b] (K)	Top Column (K)	Radiometric Accuracy (K)	Reference Pressure (K)	Spectroscopy (K)	CO_2 Variability (K)	Forward Model (K)
60–70	6.6	3.6	5.5	5.3	1.0	0.7	0.6	0.3	0.4
50–60	3.0	2.1	2.1	1.6	0.6	0.5	0.4	0.2	0.3
40–50	1.9	1.6	1.0	0.7	0.5	0.3	0.2	0.1	0.2
30–40	1.8	1.4	1.1	0.5	0.4	0.9	0.4	0.2	0.2
20–30	1.6	1.5	0.6	0.3	0.5	0.3	0.1	0.1	0.2
10–20	3.1	2.9	1.1	0.0	0.9	0.1	0.1	0.0	0.4

[a]Total error estimated as root mean square of noise and systematic errors.
[b]Systematic errors estimated as root mean square of individual retrieval errors due to uncertainties in top column data, radiometric calibration, reference pressure, spectroscopic data, carbon dioxide abundance, and forward model calculations.

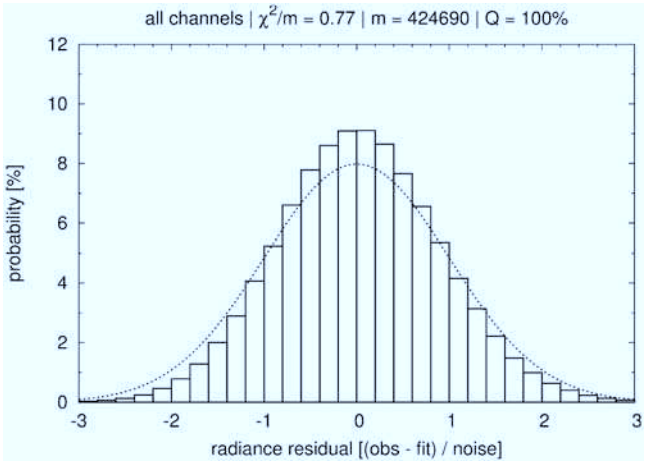

Figure 7. Histogram of normalized radiance residuals between real AIRS measurements (obs) and retrieved measurements (fit). The standard normal distribution is shown for comparison (dotted). Plot title specifies the normalized residual squared sum (χ^2/m), the number of measurements (m), and the Q-value of the χ^2-test. Analyses shown here cover a tropical AIRS granule measured at 29°S to 5°S and 118°E to 140°E on 12 January 2003, 16:42 UTC. Other granules show similar results.

granule discussed in more detail in section 5.5 of the article. The plot also shows the standard normal distribution for comparison. The histogram indicates that the AIRS noise is well characterized by a Gaussian distribution. There is no significant bias present in the residuals (the bias is about 0.03). The standard deviation of about 0.88 indicates that noise is slightly overestimated. We analyzed the residual histograms of another 35 globally distributed AIRS granules and found similar results.

[39] A standard χ^2-test is applied to determine significance [e.g., *von Clarmann*, 2006]. The χ^2-test allows identification of abnormally poor fits, that is, retrievals where the forward model simulations and radiance measurements are inconsistent with respect to measurement error (noise). The test used here is conservative because it neglects the fact that the retrieval covariance and measurement error covariance are correlated [*Rodgers*, 2000]. However, a χ^2-test based on the proper covariance is impractical due to the enhanced computational effort. The χ^2-test shows that the retrieved measurements are consistent with the real AIRS measurements with Q-values larger than 99.9%.

5.2. Consistency of the Retrieval With the a Priori Data

[40] For internal validation we check the consistency of the new temperature retrievals presented in this study with the AIRS operational retrievals which are used as a priori in our analyses. For this purpose we directly compute the temperature differences between our retrieved profiles for each individual footprint and the corresponding operational results based on the 3 × 3 combined AIRS footprints. The mean differences and standard deviations for a set of 35 globally distributed AIRS granules are shown in Figure 8. The AIRS operational temperature retrievals are carefully validated [e.g., *Fetzer et al.*, 2003; *Divakarla et al.*, 2006; *Tobin et al.*, 2006b]. Since our retrievals are nearly free of a priori information, the comparison allows to directly identify potential bias in the results. Figure 8 shows that the mean temperature difference between our results and the operational data is −2.9 to 1.9 K at 20 to 60 km altitude. These differences are in the order of the estimated systematic retrieval errors and we conclude that no significant biases are present. The standard deviation of the temperature differences are 2.2 K to 5.8 K in the same altitude range. Concerning the standard deviations, it must be taken into account that our retrievals better cover the atmospheric variability due to the enhanced horizontal resolution. Most of the selected AIRS granules have a high temperature variability due to strong gravity wave events (see sections 5.4 and 5.5). A cross-check for a subset of granules with low atmospheric variability shows significantly lower bias and standard deviations.

5.3. Comparison With ECMWF Operational Analyses

[41] We utilize pressure and temperature information from European Centre for Medium-Range Weather Forecasts (ECMWF) operational analyses (T511 grid, 0.5° × 0.5° horizontal resolution, 28 equidistant vertical levels in between 0–65 km) for a comparison. The ECMWF data are interpolated on the locations of the individual AIRS footprints and directly compared with the new temperature retrievals presented in this study. The results are summarized in Figure 8. The mean temperature differences between our retrievals and ECMWF are −3.0 to 3.5 K at 20 to 60 km altitudes. The standard deviations are 2.5 to 7.2 K in the same vertical range. The AIRS operational results compare somewhat better to ECMWF analyses. The bias varies from −0.5 to 1.7 K. The standard deviations are 1.2 to 4.4 K. As in the comparison with the a priori data it must be taken into account that the new retrievals presented here have a higher horizontal resolution and better cover the atmospheric variability. The horizontal resolution of the ECMWF data is similar to the AIRS operational retrievals.

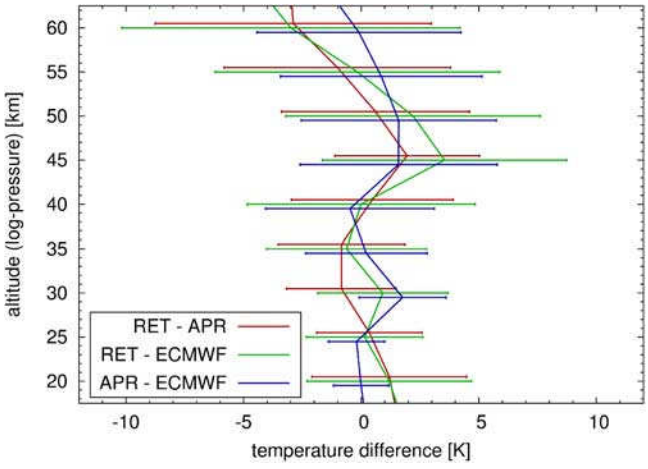

Figure 8. Comparison of temperature profiles for a set of 35 AIRS granules. Curves denote the bias, and error bars denote the standard deviations. The comparison covers the retrieval results of this study (RET), the AIRS operational Level 2 retrievals or a priori (APR), and ECMWF operational analyses (see legend).

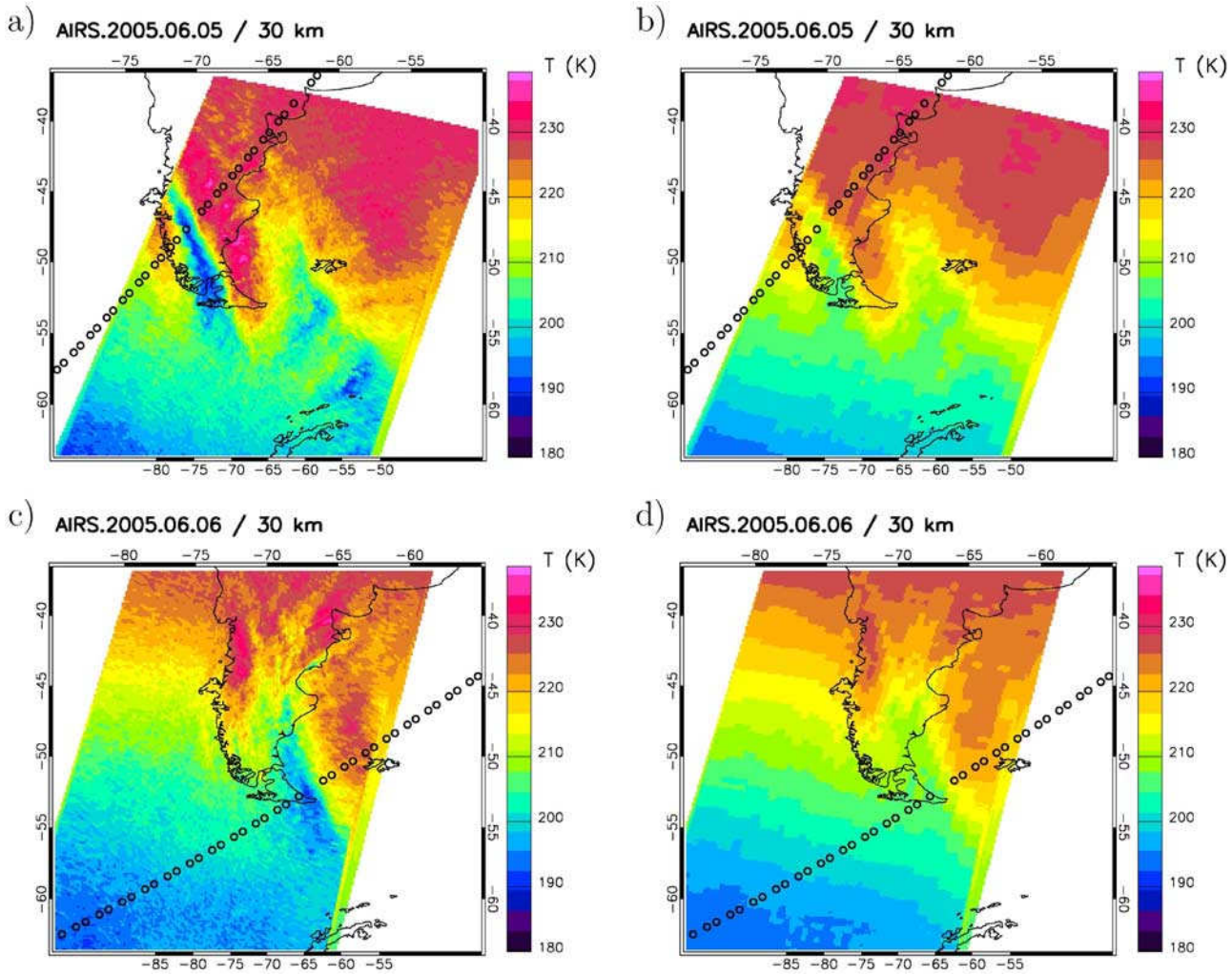

Figure 9. AIRS temperature measurements at 30 km altitude obtained on (a, b) 5 June 2005, 04:59 UTC and (c, d) 6 June 2005, 05:41 UTC near South America. Shown in Figures 9a and 9c are the results of the new retrieval scheme presented in this article and in Figures 9b and 9d are the results from the NASA operational Level 2 retrieval. Black circles indicate the coincident HIRDLS measurement tracks used for comparison.

The vertical resolution of ECMWF data are generally better than the AIRS retrievals.

5.4. Comparison With HIRDLS Satellite Measurements

[42] As described in the introduction, the primary motivation for our work is to retrieve the small-scale temperature fluctuations due to gravity waves that are missing or only poorly resolved in the AIRS operational retrievals. Here we compare gravity waves in our AIRS full-resolution retrievals to gravity waves observed at the same locations and similar times by the HIRDLS instrument that flies on the Aura satellite. Both AIRS and HIRDLS fly in the A-Train constellation of NASA satellites, so the two satellites, Aqua and Aura pass over the same geographic locations within minutes of each other. However, AIRS views in the nadir and near-nadir, while HIRDLS views the limb at an azimuth angle of 46° from the satellite orbit track. The HIRDLS measurement track is therefore displaced geographically from the AIRS track on any given orbit by a distance approximating the spacing between orbits (~24° of longitude). HIRDLS and AIRS therefore view the same geographic location at times separated by approximately 100 minutes.

[43] Gravity waves can have high frequencies and fast group velocities. The wave patterns can therefore change dramatically on timescales of 100 minutes. We focus here on comparisons between AIRS and HIRDLS observations of mountain wave events. Mountain waves are stationary relative to the ground so their geographic location and phase structure is more likely to remain constant in a 100-minute interval than waves from other sources. Mountain wave events may also last for large fractions of a day or several days at a time, whereas other sources, convection in particular, may change dramatically on timescales of minutes to hours. From HIRDLS measurements, we can obtain a vertical cross-section of wave temperature fluctuations along the measurement track [*Alexander et al.*, 2008]. To compare our full-resolution AIRS retrievals to HIRDLS, we choose AIRS swaths on adjacent orbits that cover the

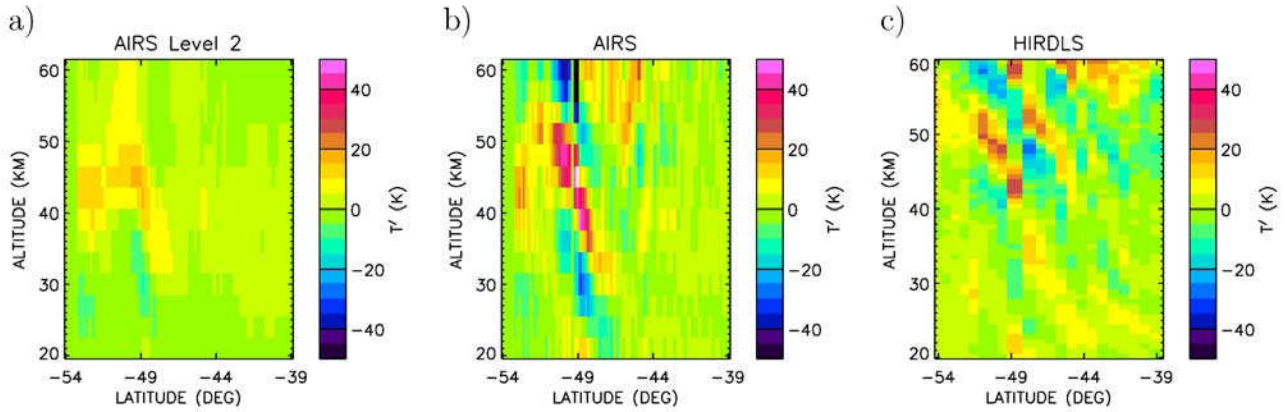

Figure 10. Cross-sections of temperature perturbations derived from (a) AIRS operational retrievals, (b) new AIRS retrievals presented in this study, and (c) HIRDLS measurements on 5 June 2005, 04:59 UTC near South America. See Figure 9a for measurement locations.

same geographic region where a mountain wave event is observed in HIRDLS, and we interpolate the AIRS three-dimensional retrievals to locations along the HIRDLS measurement track. The AIRS retrievals are first interpolated to a log-pressure vertical grid ($z_p = 7\ \text{km} \cdot \ln[1000\ \text{hPa}/p]$) for comparison to the HIRDLS measurements. Figure 9 shows the plan view of the AIRS full-resolution retrievals at z_p = 30 km and the HIRDLS measurement locations that intersect the AIRS swath. We focus on two days 5–6 June 2005 and select the nighttime overpasses.

[44] Figures 10 and 11 show side-by-side comparisons of the HIRDLS measurements and the interpolated AIRS full-resolution retrieval minus the background temperature (defined as a function of latitude smoothed over ±5° latitude) as vertical cross-sections along the line forming the HIRDLS measurement track. The interpolation is two-dimensional bilinear in the horizontal and performed independently at each AIRS level. The comparison shows excellent agreement in the phase structure and amplitude of the mountain wave events observed in the HIRDLS and AIRS temperature retrievals. HIRDLS has much higher vertical resolution (1.2 km) than AIRS, but the vertical wavelength for these wave events is long enough to be clearly observed in both. Differences between the two are most prominent where the vertical wavelength observed by HIRDLS is shorter, for example at the higher altitudes between 55°S and 50.5°S latitude on 6th June. Figures 10 and 11 also show the interpolated vertical cross-section of the operational AIRS Level 2 retrieval for these two events again with the background temperature as defined above subtracted. The wave events are severely attenuated in the operational Level 2 data. Clearly our new full-resolution retrieval is far superior than the operational retrieval for gravity wave studies.

[45] Figure 12 shows vertical profiles from the AIRS temperature retrievals sampled at the location of the HIRDLS profiles on 6 June 2005 in the center of the mountain wave event. Adjacent profiles are offset by 20 K for clarity. The coarser AIRS vertical resolution is very obvious in this format. Both the amplitudes and phase structures of the wave event are well matched in both data sets between ~20–45 km where the AIRS resolution is best. The AIRS retrieval shows the effect of the loss of vertical resolution at the higher altitudes near 50 km that was previously illustrated with Figures 5 and 6. For waves with vertical wavelengths of ~20 km or longer, the AIRS retrieval shows very nearly identical wave structure as in the HIRDLS temperature profiles in the stratosphere. The AIRS retrievals conversely have much higher horizontal resolu-

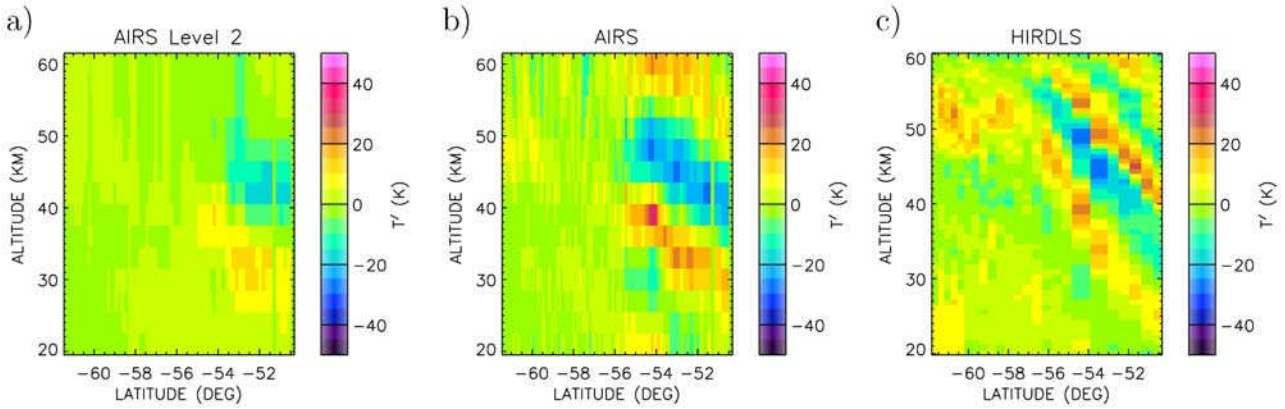

Figure 11. Cross-sections of temperature perturbations derived from (a) AIRS operational retrievals, (b) new AIRS retrievals presented in this study, and (c) HIRDLS measurements on 6 June 2005, 05:41 UTC near South America. See Figure 9c for measurement locations.

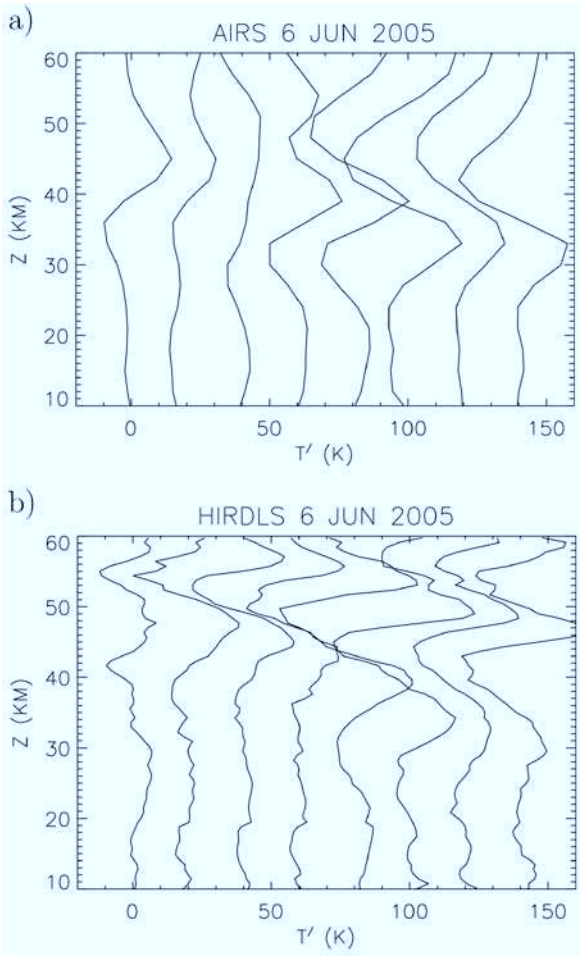

Figure 12. Temperature vertical profiles from (a) AIRS and (b) HIRDLS retrievals. Profiles are located in the center of the 6 June 2005 mountain wave event along the HIRDLS measurement track shown in Figure 9b. Adjacent temperature profiles are offset by 20 K.

tion than HIRDLS. The two measurement types, limb and nadir sounding, will therefore provide complimentary information since they cover distinctly different, but overlapping, regions of the vertical-horizontal wavelength parameter space filled by gravity waves. They therefore sample different portions of the wave intrinsic frequency spectrum as well. See the study by *Preusse et al.* [2008] for a comparison of sampling capacities with other experiments.

5.5. Observations of Small-Scale Gravity Waves

[46] Because of the enhanced horizontal resolution the new temperature data set presented here has a great potential for studies of small-scale stratospheric gravity waves. As an example, Figure 13 shows a small-scale gravity wave event observed by AIRS on 12 January 2003, 16:40 UTC near Darwin, Australia. Next to large waves fronts visible throughout the extent of the granule, the temperature perturbation maps show gravity waves induced by deep convection near 12 to 15°S and 130 to 133°E. These waves are best observed around 30 to 40 km altitude, but become less visible near 50 km altitude. Wavefronts are propagating away from a localized source in eastward direction. The horizontal wavelength is about 100 km. A. W. Grimsdell et al. (Model study of waves generated by convection with direct validation via satellite, manuscript in preparation, 2008) were able to show, that the waves observed here are indeed caused by deep convection.

[47] Comparing the retrieval results obtained in this study with results of the AIRS operational retrieval scheme, it becomes clear that the loss in horizontal resolution due to the cloud-clearing process in the operational scheme is a clear drawback for gravity wave studies. Comparing the temperature residual maps for 42 km in Figures 13b and 13c shows that the AIRS operational retrieval is not able to capture the small-scale gravity waves at all. Likewise, it also seems not to be able to capture the larger-scale waves westward of the deep convection event. For another comparison we sampled data from ECMWF operational analyses on the AIRS measurement grid and derived temperature perturbations based on the sampled data set. However, the

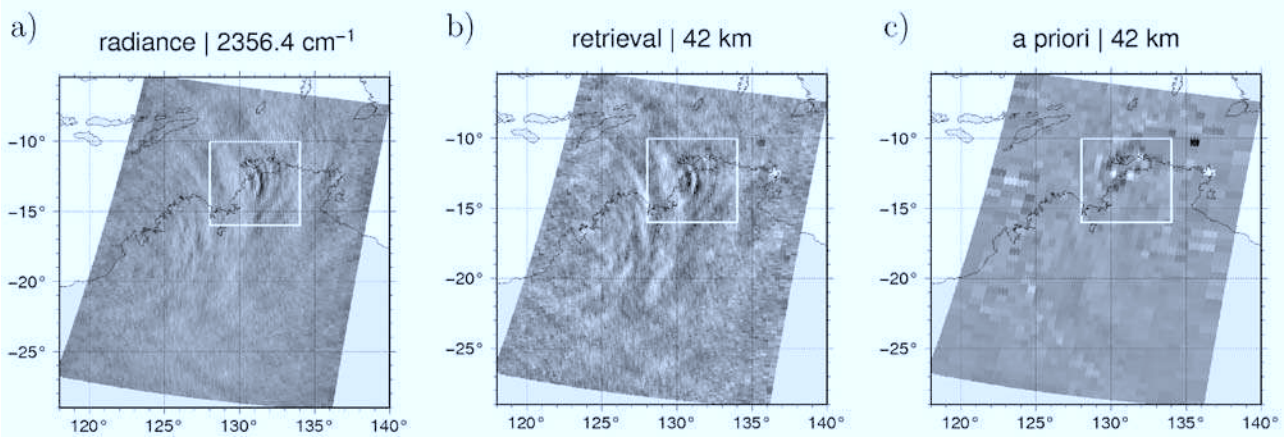

Figure 13. Small-scale gravity waves induced by deep convection as observed by AIRS on 12 January 2003, 16:42 UTC near Darwin, Australia (white box). (a) Radiance perturbations for one of the 4 μm temperature channels. The gray scale covers a range of ±15%. (b) Temperature perturbations at 42 km altitude derived from the new retrievals presented in this study. (c) Corresponding results based on AIRS operational retrieval results. For temperature perturbation plots, the gray scale covers a range of ±12.5 K.

ECMWF temperature perturbations found are below ±1.5 K and cannot be reasonably compared to our results. Figures 13b to 13c indicate that our high-resolution data have indeed a much higher variability than the AIRS operational retrievals or ECMWF analyses (compare sections 5.2 and 5.3).

[48] The small-scale wave structures found in our retrieval results are clearly present in the AIRS radiance measurements as indicated in Figure 13a. This plot shows radiance perturbation in the 2356 cm^{-1} temperature channel. The weighting function of this channel peaks around 40 km (Table 2). The relative perturbations are in the order of 10 to 15%. A 1 K temperature perturbation typically causes a 5% change in Planck radiance at 4 μm. This leads to an estimate of 2 to 3 K for the wave amplitudes, contradicting the retrieval results. However, it must be considered that the wave amplitudes get damped by the observational filter. On the basis of a vertical wavelength of about 30 km, the forward model response study presented in section 3.4 shows that the radiance response to a 1 K wave perturbation is about 1%. This leads to an estimate of 10 to 15 K for the real wave amplitudes which agrees well with the retrieval results (Figure 13b).

6. Conclusions

[49] AIRS radiance measurements are well-suited to retrieve three-dimensional high spatial resolution temperature fields in the stratosphere. We present a newly developed retrieval scheme based on a rapid radiative transfer model and an accompanying optimal estimation retrieval processor. The total error of the retrieved temperatures is 1.6 to 3.0 K in the altitude range 20 to 60 km. The retrieval noise is the leading error component (1.4 to 2.1 K). Weaker gravity waves cannot be seen in the new data set due to the noise, but there are many events with larger amplitudes than the noise. Retrieval results typically contain less than 1 to 2% a priori information. The vertical resolution of the observations is 7 to 15 km. The horizontal sampling is 13.5×20 km^2 at nadir and grows to 22×45 km^2 at edge of scan (±49.5°). First validation activities, that is, checks of internal quality measures and comparisons with ECMWF operational analyses suggest that the retrieved temperature data are reliable and well suited for further scientific studies. Data and software from this project will be made available to interested colleagues.

[50] The new data sets presented here have a great potential to study stratospheric gravity waves. This is illustrated by the presentation of AIRS observations of small-scale gravity waves induced by deep convection near Darwin, Australia on 12 January 2003 and a comparison of AIRS and HIRDLS observations of a stationary mountain wave near southern South America on 5–6 June 2005. The wave structures found in our retrievals and the HIRDLS retrievals are virtually absent in the AIRS operational analysis. For waves with vertical wavelengths of ~20 km or longer, our AIRS retrieval shows nearly identical wave structure as in the HIRDLS temperature profiles in the stratosphere. In addition, the three-dimensional temperature fields from AIRS allow us to derive the horizontal orientation of the phase fronts which is an essential information to accurately derive gravity wave momentum flux.

[51] **Acknowledgments.** Support for this work was provided by the NASA program Earth System Science Research using Data and Products from TERRA, AQUA, and ACRIM Satellites, contracts NNH04CC54C and NNH08AH43I, through Program Director Ramesh Kakar. We thank Anu Dudhia, University of Oxford, for providing the Reference Forward Model. We thank Chris Barnet, National Oceanographic and Atmospheric Administration, and L. Larrabee Strow, University of Maryland, Baltimore County, for their assistance.

References

Alexander, M. J., and C. D. Barnet (2007), Using satellite observations to constrain gravity wave parameterizations for global models, *J. Atmos. Sci.*, *64*(5), 1652–1665.

Alexander, M. J., and H. Teitelbaum (2007), Observation and analysis of a large amplitude mountain wave event over the antarctic peninsula, *J. Geophys. Res.*, *112*, D21103, doi:10.1029/2006JD008368.

Alexander, M. J., et al. (2008), Global estimates of gravity wave momentum flux from high resolution dynamics limb sounder observations, *J. Geophys. Res.*, *113*, D15S18, doi:10.1029/2007JD008807.

Aumann, H. H., D. T. Gregorich, S. L. Gaiser, D. F. Hagan, T. S. Pagano, L. L. Strow, and D. Ting (2000), AIRS level 1b algorithm theoretical basis document (ATBD) part 1 (IR), *Tech. Rep.*, NASA. (Available at http://eospso.gsfc.nasa.gov/eos_homepage/for_scientists/atbd)

Aumann, H. H., et al. (2003), AIRS/AMSU/HSB on the Aqua mission: Design, science objective, data products, and processing systems, *IEEE Trans. Geosci. Remote Sens.*, *41*, 253–264.

Aumann, H. H., D. Gregorich, and S. Gaiser (2005), AIRS hyper-spectral measurements for climate research: Carbon dioxide and nitrous oxide effects, *Geophys. Res. Lett.*, *32*, L05806, doi:10.1029/2004GL021784.

Aumann, H. H., S. Broberg, D. Elliott, S. Gaiser, and D. Gregorich (2006), Three years of Atmospheric Infrared Sounder radiometric calibration validation using sea surface temperatures, *J. Geophys. Res.*, *111*, D16S90, doi:10.1029/2005JD006822.

Barnet, C., S. Datta, and L. Strow (2003), Trace gas measurements from the Atmospheric Infrared Sounder (AIRS), paper OWB2 presented at Optical Remote Sensing, OSA Technical Digest, Quebéc City, Que., Canada, 3 Feb.

Cho, C., and D. H. Staelin (2006), Cloud clearing of Atmospheric Infrared Sounder hyperspectral infrared radiances using stochastic methods, *J. Geophys. Res.*, *111*, D09S18, doi:10.1029/2005JD006013.

Ciddor, P. E. (1996), Refractive index of air: New equations for the visible and near infrared, *Appl. Opt.*, *35*, 1566–1573.

de Souza-Machado, S., L. L. Strow, S. E. Hannon, H. Motteler, M. López-Puertas, B. Funke, and D. P. Edwards (2006), Fast forward radiative transfer modeling of 4.3 μm non-local thermodynamic equilibrium effects for the Aqua/AIRS infrared temperature sounder, *Geophys. Res. Lett.*, *34*, L01802, doi:10.1029/2006GL026684.

Divakarla, M. G., C. D. Barnet, M. D. Goldberg, L. M. McMillin, E. Maddy, W. Wolf, L. Zhou, and X. Liu (2006), Validation of Atmospheric Infrared Sounder temperature and water vapor retrievals with matched radiosonde measurements and forecasts, *J. Geophys. Res.*, *111*, D09S15, doi:10.1029/2005JD006116.

Dudhia, A. (2003), Temperature soundings, in *Encyclopedia of Atmospheric Sciences*, pp. 1985–1998, Elsevier, New York.

Dudhia, A. (2004), *RFM Software User's Manual*, Department of Atmospheric, Oceanic and Planetary Physics, Univ. of Oxford, Oxford, U. K. (Available at http://www.atm.ox.ac.uk/RFM)

Dudhia, A., P. E. Morris, and R. J. Wells (2002), Fast monochromatic radiative transfer calculations for limb sounding, *J. Quant. Spectrosc. Radiat. Transfer*, *74*, 745–756.

Eckermann, S. D., and P. Preusse (1999), Global measurements of stratospheric mountain waves from space, *Science*, *286*, 5444, 1534–1537.

Eckermann, S. D., J. Ma, D. L. Wu, and D. Broutman (2007), A three-dimensional mountain wave imaged in satellite radiance throughout the stratosphere: Evidence of the effects of directional wind shear, *Q. J. R. Meteorol. Soc.*, *133*, 1959–1975.

Ern, M., P. Preusse, M. J. Alexander, and C. D. Warner (2004), Absolute values of gravity wave momentum flux derived from satellite data, *J. Geophys. Res.*, *109*, D20103, doi:10.1029/2004JD004752.

Ern, M., P. Preusse, and C. D. Warner (2006), Some experimental constraints for spectral parameters used in the Warner and McIntyre gravity wave parameterization scheme, *Atmos. Chem. Phys.*, *6*, 4361–4381.

Eyring, V., et al. (2007), Multimodel projections of stratospheric ozone in the 21st century, *J. Geophys. Res.*, *112*, D16303, doi:10.1029/2006JD008332.

Fetzer, E. J. (2006), Preface to special section: Validation of Atmospheric Infrared Sounder observations, *J. Geophys. Res.*, *111*, D09S01, doi:10.1029/2005JD007020.

Fetzer, E. J., and J. C. Gille (1994), Gravity wave variance in LIMS temperatures, part i: Variability and comparison with background winds, *J. Atmos. Sci.*, *51*, 2461–2483.

Fetzer, E., et al. (2003), AIRS/AMSU/HSB validation, in *IEEE Trans. Geosci. Remote Sens.*, vol. 41, pp. 418–431.

Francis, G. L., D. P. Edwards, A. Lambert, C. M. Halvorson, J. M. Lee-Taylor, and J. C. Gille (2006), Forward modeling and radiative transfer for the NASA EOS-Aura High Resolution Dynamics Limb Sounder (HIRDLS) instrument, *J. Geophys. Res.*, *111*, D13301, doi:10.1029/2005JD006270.

Fritts, D. C., and M. J. Alexander (2003), Gravity wave dynamics and effects in the middle atmosphere, *Rev. Geophys.*, *41*(1), 1003, doi:10.1029/2001RG000106.

Gille, J. C., J. J. Barnett, J. G. Whitney, M. A. Dials, D. Woodard, W. P. Rudolf, A. Lambert, and W. Mankin (2003), The High-Resolution Dynamics Limb Sounder (HIRDLS) experiment on Aura, *Proc. SPIE*, *5152*, 161–171.

Gille, J., et al. (2008), High Resolution Dynamics Limb Sounder: Experiment overview, recovery, and validation of initial temperature data, *J. Geophys. Res.*, *113*, D16S43, doi:10.1029/2007JD008824.

Goldberg, M. D., Y. Qu, L. M. McMillin, W. Wolf, L. Zhou, and M. Divakarla (2003), AIRS near-real-time products and algorithms in support of numerical weather prediction, *IEEE Trans. Geosci. Remote Sens.*, *41*, 379–389.

Gordley, L. L., and J. M. Russel (1981), Rapid inversion of limb radiance data using an emissivity growth approximation, *Appl. Opt.*, *20*, 807–813.

Hase, F., and M. Höpfner (1999), Atmospheric ray path modeling for radiative transfer algorithms, *Appl. Opt.*, *38*, 3129–3133.

Hoffmann, L. (2006), Schnelle Spurengasretrieval für das Satellitenexperiment Envisat MIPAS, *Tech. Rep. JUEL-4207*, Forschungszentrum Jülich, Juelich, Germany.

Hoffmann, L., M. Kaufmann, R. Spang, R. Müller, J. J. Remedios, D. P. Moore, C. M. Volk, T. von Clarmann, and M. Riese (2008), Envisat MIPAS measurements of CFC-11: Retrieval, validation, and climatology, *Atmos. Chem. Phys.*, *8*, 3671–3688.

Lindzen, R. (1973), Wave-mean flow interactions in the upper atmosphere, *Boundary Layer Meteorol.*, *4*, 327–343.

Marshall, B. T., L. L. Gordley, and D. A. Chu (1994), BANDPAK: Algorithms for modeling broadband transmission and radiance, *J. Quant. Spectrosc. Radiat. Transfer*, *52*, 581–599.

Nalli, N. R., et al. (2006), Ship-based measurements for infrared sensor validation during Aerosol and Ocean Science Expedition 2004, *J. Geophys. Res.*, *111*, D09S04, doi:10.1029/2005JD006385.

Pagano, T. S., H. H. Aumann, D. E. Hagan, and K. Overoye (2003), Prelaunch and in-flight radiometric calibration of the Atmospheric Infrared Sounder (AIRS), *IEEE Trans. Geosci. Remote Sens.*, *41*, 265–273.

Parkinson, C. L. (2003), Aqua: An Earth-observing satellite mission to examine water and other climate variables, *IEEE Trans. Geosci. Remote Sens.*, *41*, 173–183.

Preusse, P., S. D. Eckermann, and D. Offermann (2000), Comparison of global distributions of zonal-mean gravity wave variance inferred from different satellite instruments, *Geophys. Res. Lett.*, *27*, 3877–3880.

Preusse, P., A. Dörnbrack, S. D. Eckermann, M. Riese, B. Schaeler, J. T. Bacmeister, D. Broutman, and K. U. Grossmann (2002), Space-based measurements of stratospheric mountain waves by CRISTA: 1. sensitivity, analysis method, and a case study, *J. Geophys. Res.*, *107*(D23), 8178, doi:10.1029/2001JD000699.

Preusse, P., S. D. Eckermann, and M. Ern (2008), Transparency of the atmosphere to short horizontal wavelength gravity waves, *J. Geophys. Res.*, *113*, D24104, doi:10.1029/2007JD009682.

Remedios, J. J., R. J. Leigh, A. M. Waterfall, D. P. Moore, H. Sembhi, I. Parkes, J. Greenhough, M. Chipperfield, and D. Hauglustaine (2007), MIPAS reference atmospheres and comparisons to V4.61/V4.62 MIPAS Level 2 geophysical data sets, *Atmos. Chem. Phys. Discuss.*, *7*, 9973–10,017.

Rodgers, C. D. (1976), Retrieval of atmospheric temperature and composition from remote measurements of thermal radiation, *Rev. Geophys. Space Phys.*, *14*, 609–624.

Rodgers, C. D. (1990), Characterization and error analysis of profiles retrieved from remote sounding measurements, *J. Geophys. Res.*, *95*, 5587–5595.

Rodgers, C. D. (1998), Information content and optimization of high spectral resolution remote measurements, *Adv. Space Res.*, *21*, 361–367.

Rodgers, C. D. (2000), *Inverse Methods for Atmospheric Sounding: Theory and Practice*, *Series on Atmospheric, Oceanic and Planetary Physics*, vol. 2, World Sci., Hackensack, N. J.

Rosenkranz, P. W. (2003), Rapid radiative transfer model for AMSU/HSB channels, *IEEE Trans. Geosci. Remote Sens.*, *41*, 362–368.

Rothman, L. S., et al. (2003), The HITRAN molecular spectroscopic database: Edition of 2000 including updates through 2001, *J. Quant. Spectrosc. Radiat. Transfer*, *82*, 5–44.

Schoeberl, M. R., et al. (2004), Earth observing missions benefit atmospheric research, *Eos Trans. AGU*, *85*(18), 177, doi:10.1029/2004EO180001.

Spang, R., G. Eidmann, M. Riese, D. Offermann, P. Preusse, L. Pfister, and P.-H. Wang (2002), CRISTA observations of cirrus clouds around the tropopause, *J. Geophys. Res.*, *107*(D23), 8174, doi:10.1029/2001JD000698.

Strow, L. L., S. E. Hannon, S. De Souza-Machado, H. E. Motteler, and D. Tobin (2003), An overview of the AIRS radiative transfer model, *IEEE Trans. Geosci. Remote Sens.*, *41*, 303–313.

Strow, L. L., S. E. Hannon, S. de-Souza Machado, H. E. Motteler, and D. C. Tobin (2006), Validation of the Atmospheric Infrared Sounder radiative transfer algorithm, *J. Geophys. Res.*, *111*, D09S06, doi:10.1029/2005JD006146.

Susskind, J., C. D. Barnett, and J. M. Blaisdell (2003), Retrieval of atmospheric and surface parameters from AIRS/AMSU/HSB data in the presence of clouds, *IEEE Trans. Geosci. Remote Sens.*, *41*, 390–409.

Susskind, J., C. Barnet, J. Blaisdell, L. Iredell, F. Keita, L. Kouvaris, G. Molnar, and M. Chahine (2006), Accuracy of geophysical parameters derived from Atmospheric Infrared Sounder/Advanced Microwave Sounding Unit as a function of fractional cloud cover, *J. Geophys. Res.*, *111*, D09S17, doi:10.1029/2005JD006272.

Tobin, D. C., et al. (2006a), Radiometric and spectral validation of Atmospheric Infrared Sounder observations with the aircraft-based scanning high-resolution interferometer sounder, *J. Geophys. Res.*, *111*, D09S02, doi:10.1029/2005JD006094.

Tobin, D. C., et al. (2006b), Atmospheric radiation measurement site atmospheric state best estimates for Atmospheric Infrared Sounder temperature and water vapor retrieval validation, *J. Geophys. Res.*, *111*, D09S14, doi:10.1029/2005JD006103.

Tsuda, T., M. Nishida, C. Rocken, and R. H. Ware (2000), A global morphology of gravity wave activity in the stratosphere revealed by the GPS occultation data (GPS/MET), *J. Geophys. Res.*, *105*, 7257–7274.

von Clarmann, T. (2006), Validation of remotely sensed profiles of atmospheric state variables: Strategies and terminology, *Atmos. Chem. Phys.*, *6*, 4311–4320.

von Clarmann, T., and G. Echle (1998), Selection of optimized microwindows for atmospheric spectroscopy, *Appl. Opt.*, *37*, 7661–7669.

von Clarmann, T., U. Grabowski, and M. Kiefer (2001), On the role of nonrandom errors in inverse problems in radiative transfer and other applications, *J. Quant. Spectrosc. Radiat. Transfer*, *71*, 39–46.

Walden, V. P., W. L. Roth, R. S. Stone, and B. Halter (2006), Radiometric validation of the Atmospheric Infrared Sounder over the Antarctic plateau, *J. Geophys. Res.*, *111*, D09S03, doi:10.1029/2005JD006357.

Wang, P.-H., P. Minnis, M. P. McCormick, G. S. Kent, and K. M. Skeens (1996), A 6-year climatology of cloud occurrence frequency from stratospheric aerosol and gas experiment ii observations (1985–1990), *J. Geophys. Res.*, *101*, 29,407–29,430.

Weinreb, M. P., and A. C. Neuendorffer (1973), Method to apply homogeneous-path transmittance models to inhomogenous atmospheres, *J. Atmos. Sci.*, *30*, 662–666.

Wu, D. L. (2004), Mesoscale gravity wave variances from AMSU-A radiances, *Geophys. Res. Lett.*, *31*, L12114, doi:10.1029/2004GL019562.

Wu, D. L., and J. W. Waters (1996), Gravity-wave-scale temperature fluctuations seen by the UARS MLS, *Geophys. Res. Lett.*, *23*, 3289–3292.

Wu, D. L., P. Preusse, S. D. Eckermann, J. H. Jiang, M. de la Torre Juarez, L. Coy, B. Lawrence, and D. Y. Wang (2006), Remote sounding of atmospheric gravity waves with satellite limb and nadir techniques, *Adv. Space Res.*, *37*, 2269–2277.

M. J. Alexander, Colorado Research Associates Division, NorthWest Research Associates, Inc., 3380 Mitchell Lane, Boulder, CO 80301, USA. (alexand@cora.nwra.com)

L. Hoffmann, Institut für Chemie und Dynamik der Geosphäre, Forschungszentrum Jülich GmbH, Leo-Brandt-Str. 2, D-52425 Juelich, Germany. (l.hoffmann@fz-juelich.de)